PET/MRI of inflammation in myocardial infarction

Won Woo Lee, MD PhD[*,1,2], **Brett Marinelli, BS**[*,1], **Anja M. van der Laan, MD**[3], **Brena Sena, BS**[1], **Rostic Gorbatov, BS**[1], **Florian Leuschner, MD**[1], **Partha Dutta, PhD**[1], **Yoshiko Iwamoto, BS**[1], **Takuya Ueno, MD PhD**[1], **Mark P.V. Begieneman, BS**[4], **Hans W.M. Niessen, MD, PhD**[4], **Jan J. Piek, MD**, **Claudio Vinegoni, PhD**[1], **Mikael J. Pittet, PhD**[1], **Filip K. Swirski, PhD**[1], **Ahmed Tawakol, MD**[5], **Marcelo Di Carli, MD**[6], **Ralph Weissleder, MD PhD**[1], and **Matthias Nahrendorf, MD PhD**[1]

[1]Center for Systems Biology, Massachusetts General Hospital and Harvard Medical School, Simches Research Building, 185 Cambridge St., Boston, MA 02114 [2]Department of Nuclear Medicine, Seoul National University Bundang Hospital, Seoul National University College of Medicine, 166 Gumi-ro, Bundang-gu, Seongnam-si, Gyeonggi-do 463-707 Korea [3]Department of Cardiology, Academic Medical Center, University of Amsterdam, Amsterdam, The Netherlands [4]Department of Pathology and Cardiac Surgery, ICaR-VU, VU University Medical Center, Amsterdam, The Netherlands [5]Cardiac MR PET CT Program, Division of Cardiology and Department of Radiology, Massachusetts General Hospital [6]Division of Nuclear Medicine and Molecular Imaging, Department of Radiology, Brigham and Women's Hospital, 75 Francis Street, Boston, MA 02115

Abstract

Objectives—The aim of this study was to explore post-MI myocardial inflammation.

Background—Innate immune cells are centrally involved in infarct healing and are emerging therapeutic targets in cardiovascular disease, however; clinical tools to assess their presence in tissue are scarce. Furthermore, it is currently not known if the non-ischemic remote zone recruits monocytes.

Methods—Acute inflammation was followed in mice with coronary ligation by ^{18}FDG PET/ MRI, FACS, PCR and histology.

Results—Gd-DTPA enhanced infarcts showed high ^{18}FDG uptake on day 5 after MI. Cell depletion and isolation data confirmed that this largely reflected inflammation; CD11b$^+$ cells had 4-fold higher ^{18}FDG uptake than the infarct tissue from which they were isolated (*P*<0.01). Surprisingly, there was considerable monocyte recruitment in the remote myocardium (~10^4/mg myocardium, 5.6-fold increase, *P*<0.01), a finding mirrored by macrophage infiltration in remote myocardium of patients with acute MI. Temporal kinetics of cell recruitment were slower than in the infarct, with peak numbers on day 10 after ischemia. Quantitative PCR showed robust increase of recruiting adhesion molecules and chemokines in remote myocardium (e.g. 12-fold increase of MCP-1), although levels were always lower than in the infarct. Finally, matrix metalloproteinase activity was significantly increased in non-infarcted myocardium, suggesting that monocyte recruitment to the remote zone may contribute to post MI dilation.

Lee: PET/MRI in acute MI

Conclusion—These studies shed light on the innate inflammatory response in remote myocardium after myocardial infarction.

Keywords

PET/MRI; myocardial infarction; inflammation; remote myocardium

INTRODUCTION

Myocardial infarction triggers a robust local inflammatory response (1, 2). On the cellular level, the innate immune system reacts to ischemic injury with mobilization of neutrophils and monocytes during the first weeks after ischemia. The amplitude and duration of inflammation and its timely resolution influence post MI remodeling and the evolution of heart failure, hence, these cells and their recruiting mechanisms are discussed as therapeutic targets. Leukocyte recruitment has been studied closely in the infarct, however; less is known about acute inflammation in the remote, non-ischemic myocardium. Given that side-to-side slippage of myocytes, myocyte hypertrophy, myocyte apoptosis and remodeling of the collagen matrix occur here and substantially contribute to the dilation of the heart after MI (3-6), the non-ischemic myocardium deserves closer scrutiny. One reason for the limited insight into inflammatory processes after MI, at least in patients, is the paucity of imaging tools to study tissue levels of inflammatory cells (7).

Emerging hybrid PET/MRI has considerable potential for cardiovascular imaging because it combines PET, a highly sensitive and quantitative modality that can follow rare molecular events (8, 9), with MRI, which non-invasively assesses cardiovascular anatomy and function, infarct size, perfusion, myocardial strain and metabolism with excellent spatial and temporal resolution (10-14). Combining both modalities could enhance preclinical research by providing multidimensional "systems" data and is also likely to directly impact clinical imaging (15-17). Here we devised a fusion method that relies on a fiducial vest developed for cardiovascular imaging in mice with separate scanners. We hypothesized that when glucose utilization is suppressed in myocytes, the temporal and spatial [18]FDG signal pattern may reflect inflammatory cell activity in the heart. We then explored the recruitment of monocytes to non-ischemic remote myocardium after coronary ligation in mice, using imaging in conjunction with flow cytometric cell quantitation.

METHODS

Please see the supplementary method section for additional information.

PET-CT

Mice were imaged by microPET/CT using an Inveon (Siemens) small animal scanner one hour after IV injection of 20.7±0.9MBq [18]FDG through the tail vein. CT preceded PET, acquiring 360 cone beam projections with a source power and current of 80keV and 500μA. Projections were reconstructed into three-dimensional volumes containing 512x512x768 voxels with the dimension of 0.11x0.11x0.11mm. Gated PET was acquired for 30 minutes using ECG leads and a respiratory pillow (M2M). A high-resolution Fourier re-binning algorithm was used to re-bin sinograms, followed by a filtered back-projection algorithm for reconstruction. Image voxel size was 0.797x0.861x0.861mm. Data were calculated as mean standardized uptake values (SUV).

MRI

We obtained delayed enhancement cine images on a 7T Bruker Pharmascan with ECG and respiratory gating (SA Instruments), a gradient echo FLASH-sequence with the following imaging parameters: echo time, 2.7ms; 16 frames per RR interval (TR 7.0-15ms); resolution 200μmx200μmx1mm; NEX 4; flip angle 60 degrees. Imaging was done 10-20 minutes after i.v. injection of 0.3 mmol/kg Gd-DTPA (19, 20).

Registration/Fusion

PET/MRI fusion was facilitated by a custom-designed mouse bed and a PET/CT gantry adapter. These hardware components facilitated intermodal transfer, minimized animal motion and allowed us to center the mouse at nearly identical coordinates in MRI and PET/CT scanners. A "framed fusion" approach was then implemented (21) using external fiducial landmarks. The fiducials were provided by a custom-built "vest" (Figure 1) made out of several loops of PE50 tubing. The vest tightly surrounded the mouse's chest, providing a rigid frame that followed movements of the animal during transfer. The tubes were filled with 15% iodine in water, rendering them visible in both CT and MRI. The tubes' orientation was optimized to provide unique landmarks for MRI and CT data registration (outlined in Figure 1). PET data were fused to CT as part of a standard PET/CT workflow. Registration of MRI and CT datasets was obtained by computing the rigid transformation necessary to superimpose the fiducials via a two-step process. The first step accomplished rough alignment of data sets based on the holder position within each modality, followed by translational and rotational alignment via a cross correlation algorithm. Fused datasets were used to place volumes of interest for quantitation of PET signal. Colocalisation achieved by this procedure was tested with a ^{18}F phantom using the cross correlation function (22). The peak correlation coefficient of 5 MRI and PET slices was 0.91±0.02, implying excellent co-registration of signal distribution between PET and MRI (Figure 2).

Clinical PET/CT was obtained on day 5 after MI after obtaining informed consent and approval of the institutional committee. To limit myocyte uptake of ^{18}FDG, patients received a high-fat, low-carbohydrate diet the evening before imaging, were fasted for 12 hours prior to imaging, and were given beta-blockers IV and a lipid-rich drink (very low carbohydrate Atkins Shake) 90 minutes prior to ^{18}FDG injection (23).

Flow cytometry was performed on days 1 to 14 post-MI (n=3-4 per group) (24). Hearts were divided into MI and remote myocardium, digested in enzyme mixture and passed through a cell strainer. Singe cell suspensions were stained with the following antibodies: CD11b-APC-Cy7, B220-PE, CD49b-PE, NK1.1-PE, CD90-PE, Ly-6G-PE, Ter119-PE, F4/80-PE-Cy7and Ly-6C-FITC (BD Biosciences). Monocytes/macrophages were defined as CD11b^{high} (B220/CD49b/NK1.1/CD90/Ly-6G/Ter119)^{low}. Monocyte subsets were identified as CD11b^{high} (B220/CD49b/NK1.1/CD90/Ly-6G/Ter119)^{low} F4/80^{low} Ly-6C^{high} or Ly-6C^{low}. Flow cytometry was performed using a multi-color flow cytometer (LSR II, BD Biosciences).

Measurement of activity in monocytes/macrophages isolated from infarcts

^{18}FDG was injected i.v. (n=6). Three hours later hearts were removed and activity in infarcts was measured by gamma counting. Afterwards, tissue was treated as above to produce cell suspensions. Cells were stained with CD11b-PE followed by incubation with anti-PE magnetic beads (Miltenyi) and separated with MACS columns. Activity of magnetically retrieved cells was measured by gamma counting.

Cx3cr1$^{gfp/+}$ mice (n=3) were used to measure the diameter of splenic monocytes (25) to calculate monocyte weight. This was necessary to compare cell and tissue activity, both

normalized to weight. In mice anesthetized with isoflurane, the spleen was imaged with intravital microscopy as previously described (26, 27) using an intravital laser scanning microscope (IV100, Olympus).

Immunohistochemistry on human myocardial tissue—Myocardial tissue was collected from patients with an infarct age of 5-14 days that were referred to the department of Pathology, VU University Medical Center, Amsterdam (n=11, male=5, age 62±16 years). Tissue was obtained from the infarct zone (left ventricle) and the remote myocardium (right ventricle). Of note, we cannot exclude that coronary arteries supplying the remote myocardium were completely free of disease in these patients. Control tissue was obtained from 8 patients who died from a cause not related to MI (n=8, male=4, age 61±16 years). None of the patients in this study received reperfusion therapy. The study was conducted in accordance with the Declaration of Helsinki, and the study protocol was approved by the institutional medical ethics committee. Tissue was fixed in formalin, embedded in paraffin, cut in 4 μm thick sections and stained with an antibody for human CD68 (Dako). Quantification of macrophages was performed by counting the number of extravascular CD68^{+} macrophages.

RESULTS

Myocardial [18]FDG signal

PET/MR images ([18]FDG PET combined with delayed enhancement MRI after injection of Gd-DTPA) and ex vivo autoradiography in conjunction with TTC staining showed that ketamine/xylazine anesthesia suppressed uptake in the remote myocardium and unmasked the increased PET signal in infarcts on day 5 after MI (Figure 3). Specifically, the infarct-to-remote-myocardium signal ratio changed from 0.33±0.1 with isoflurane to 1.56±0.1 using ketamine/xylazine (p<0.05, Figure 3G). To explore whether [18]FDG could be used to follow infarct inflammation in humans, we imaged a patient 5 days after inferior MI. In this patient, occlusive thrombosis of the right coronary artery was verified by X-ray coronary angiography and treated by placement of a stent. PET images showed increased [18]FDG signal within the inferior left ventricular wall (Figure 3H,I).

[18]FDG uptake in monocytes/macrophages

We performed several experiments to determine if monocytes/macrophages in the infarct contain [18]FDG after intravenous injection of the PET agent. First, we isolated monocytes/macrophages from infarcts and measured activity in these purified cell populations as outlined in Figure 4A. Traditionally, reported tissue activity is normalized to weight. To calculate monocyte weight using the radius, volume and density, we measured the diameter of monocytes by intravital microscopy (13.2±1.0μm, Figure 4B). The calculated average cellular weight was 1.3ng. This number was then used to normalize [18]FDG activity to weight by multiplication with the cell number in the sample. The activity of cells isolated from infarcts was significantly higher than the activity of the infarct tissue from which they were retrieved (Figure 4C). We also isolated monocyte/macrophages, endothelial cells and fibroblast from infarcts after intravenous [18]FDG injection. Scintillation counting revealed that the cellular activity was highest in monocytes/macrophages (Figure 4D).

Next, we depleted monocytes/macrophages with clodronate liposomes and imaged these mice on day 5 after MI. Depletion reduced the in vivo infarct activity by 34% (Figure 4E). Scintillation counting of infarct tissue showed a 37% decrease of activity (Figure 4E). Immunohistochemistry and flow cytometric enumeration confirmed a reduction of monocyte/macrophage numbers by 35%, comparable to the decrease in [18]FDG signal

(Figure 4F). On day 10 after MI, depletion reduced the infarct signal by 31% (n=6 per group, p<0.05).

Time course of ^{18}FDG PET signal

There was significantly increased uptake in the infarct of mice on day 5 after coronary ligation (Standard uptake value 2.7±0.1, Figure 5) when compared to myocardium in control mice (1.3±0.2, p<0.01). On day 14, the ^{18}FDG signal approached control values (MI 1.6±0.1, remote 1.4±0.1). Scintillation counting corroborated the imaging results (Figure 5). Interestingly, we found differences between the activity in non-infarcted remote myocardium on day 5 after MI and control hearts (%IDGT remote, 8.9±0.5; control, 5.1±1.0, *P*<0.05). The MRI component of hybrid data sets enabled the precise definition of the infarct area and analysis of anatomic and functional parameters. The infarct size was 30±2% in the studied cohorts. Wall thickening was reduced in the infarcted area (remote, 45±5%; infarct, 10±5%, *P*<0.01).

Monocyte/macrophage recruitment

Surprisingly, we found monocyte/macrophage recruitment in the non-infarcted remote myocardium (Figure 6A). The number of CD11b$^+$ cells counted by FACS was lower than in the infarct and reached a later peak around day 10. Immunofluorescent cell quantitation by histology corroborated these findings (Figure 6B). In some cases, monocyte/macrophages were most numerous in the border zone of the infarct (Figure 6C), which may explain why we observed the peak PET signal at the edge of large infarcts (Figure 6C).

Finding monocytes/macrophages in the non-ischemic remote zone motivated us to study chemokine and adhesion molecule expression typically involved in cell recruitment (1). mRNA of CCR2, a chemokine receptor highly expressed by monocytes, was increased 66-fold in the infarct and 9-fold in the remote zone on day 5 after MI (Figure 6D). P-Selectin, E-Selectin and VCAM-1 expression were mildly increased (Figure 6D). MCP-1, MCP-3, MCP-5 and fractalkine were also upregulated in the remote zone when compared to control myocardium from non-infarcted hearts (12-fold, 18-fold, 9-fold and 3-fold, respectively, p<0.05, Figure 6D). Immunohistochemical and immunofluorescence studies showed expression of MCP-1 and VCAM-1 in the remote zone, which co-localized with endothelial cells (Figure 7). Profiling for monocyte subsets in the remote myocardium revealed that Ly-6C^{high} monocytes were recruited early and were followed by Ly-6C^{low} monocytes, which peaked at day 10 after MI, about 5 days later when compared to cell dynamics in the infarct (Figure 8). Analysis of clinical specimen obtained from autopsy cases after acute MI revealed robust recruitment of CD68$^+$ macrophages to the non-infarcted myocardium in patients (Figure 9).

Protease activity

Finally, we assessed the activity of matrix metalloproteinases 2 and 9 using an activatable fluorescence reporter. While fluorescence was highest in the infarct, we found significant activation of the probe in the remote zone and septum (Figure 10).

DISCUSSION

The data presented here reflect the spatial and temporal kinetics of innate immune cells after myocardial infarction and explore ^{18}FDG PET for following infarct inflammation. Early after ischemia, monocytes and macrophages infiltrate injured tissue in large numbers. These innate immune cells are emerging as key regulators of infarct healing (1, 2). Previous studies have shown that monocytes/macrophages are present *in the ischemic myocardium* during the first two weeks after ischemic injury (18, 24). They remove

debris, enhance neoangiogenesis, release a myriad of inflammatory cytokines and are a major source of proteases that regulate the turnover of extracellular matrix. Preclinical studies revealed that proper infarct healing calls for a delicate balance of monocyte activity (2). Excessive as well as insufficient monocyte/macrophage numbers in the infarct compromise cardiac repair and lead to infarct expansion, aggressive left ventricular dilation and ultimately heart failure. Studies correlating the number of circulating blood pool monocytes at the time of infarction with clinical outcome suggest that the above preclinical data reflect infarct healing in patients (28-30).

While the presence, time course and function of innate immune cells in the infarct has been well described, our finding of inflammation in the remote zone is new and somewhat surprising. The amount of monocytes/macrophages in the non-infarcted myocardium was lower than in the ischemic tissue; however, their numbers detected by flow cytometry were substantial ($\sim 10^4$ per mg tissue, 5.6-fold higher than in control mice). The time course accorded with the 2 monocytic phases described in the infarct (24) but the kinetics were slower. Peak cell numbers were reached on day 10 after MI, 5 days later than in the ischemic zone. Exploring the mechanism of recruitment, we also found increased expression of adhesion molecules and the chemokines known to recruit monocytes into the infarct (1, 2). Tissue obtained from clinical autopsies showed a robust increase of macrophages in the remote myocardium of patients that died on day 5-14 after the ischemic event. The finding of higher MMP activity in the remote zone of mice indicates that these inflammatory processes are involved in remodeling of the left ventricle after ischemic injury, although the precise cellular contribution of MMP activity is unclear at this point. Future studies are required to dissect the molecular mechanism on how inflammation in the non-ischemic myocardium is triggered. The expression of recruiting molecules such as VCAM-1 and MCP-1 argues against a mere "spill over" effect from the infarct. One could speculate that apoptosis of remote myocytes may trigger cell recruitment, or that systemically increased angiotensin-2 activates endothelium in the remote zone.

We here present data showing that within sub-acutely infarcted myocardium, ^{18}FDG accumulates relative to the tissue's monocyte/macrophage content. PET signal changed synchronously with the number of innate immune cells, mirrored their typical spatial distribution after MI, and decreased in scale to cell numbers in a monocyte/macrophage depletion experiment. Furthermore, monocytes/macrophages isolated from infarcts showed high ^{18}FDG uptake. This evidence suggests that the infarct signal on day 5 after ischemia reflects -- at least in part -- inflammatory activity. Since ^{18}F decays with a half life of 110 minutes, serial non-invasive spatio-temporal imaging of inflammation appears feasible.

The use of ^{18}FDG to image inflammation in myocardium has limitations. Myocytes can metabolize glucose and therefore show high ^{18}FDG uptake. Residual viable myocytes in the infarct may contribute to signal. Accordingly, suppression of this uptake is a prerequisite for imaging of inflammatory cells. Clinically, methods suppressing myocardial uptake have been developed to image inflammation in coronary arteries (23, 31), and the clinical PET/CT case discussed in Figure 3 suggests that these strategies may also prove useful for imaging inflammation in the myocardium. Acutely ischemic and hibernating myocardium shifts its metabolic use of fatty acids towards glucose (32), which results in increased ^{18}FDG uptake and may change the observed relationship between ^{18}FDG uptake and Mφ activity. Novel PET tracers that specifically target monocytes/macrophages could overcome these limitations (33, 34), however; ^{18}FDG is clinically approved and could be explored now.

The obtained data showcase the synergy created by fusing high resolution cardiac PET with MRI. Using separate systems and off-line fusion circumvents engineering challenges faced in hybrid scanners, where deploying PET in a magnetic field currently compromises

sensitivity. Combining leading modalities for molecular and anatomic cardiovascular imaging holds promise for a number of interesting future applications. Data on cardiac metabolism, molecular pathways, cell populations or drug targets could be integrated with parameters such as myocardial motion, strain, torsion or perfusion. Such integration could foster modeling and systems biology approaches to provide novel insight into better treating heart failure.

Supplementary Material

Refer to Web version on PubMed Central for supplementary material.

Acknowledgments

ABBREVIATIONS

CT	X-ray computed tomography
FACS	flow cytometry
MI	Myocardial infarction
MRI	Magnetic Resonance Tomography
PET	Positron Emission Tomography
PCR	quantitative real time polymerase chain reaction
^{18}FDG	18-fluorodeoxyglucose

REFERENCES

1. Frangogiannis NG, Smith CW, Entman ML. The inflammatory response in myocardial infarction. Cardiovasc Res. 2002; 53:31–47. [PubMed: 11744011]

2. Nahrendorf M, Pittet MJ, Swirski FK. Monocytes: protagonists of infarct inflammation and repair after myocardial infarction. Circulation. 2010; 121:2437–45. [PubMed: 20530020]

3. Pfeffer MA, Braunwald E. Ventricular remodeling after myocardial infarction. Experimental observations and clinical implications. Circulation. 1990; 81:1161–72. [PubMed: 2138525]

4. Jourdan-Lesaux C, Zhang J, Lindsey ML. Extracellular matrix roles during cardiac repair. Life Sci. 2010; 87:391–400. [PubMed: 20670633]

5. Jugdutt BI. Ventricular remodeling after infarction and the extracellular collagen matrix: when is enough enough? Circulation. 2003; 108:1395–403. [PubMed: 12975244]

6. Anversa P, Kajstura J, Olivetti G. Myocyte death in heart failure. Curr Opin Cardiol. 1996; 11:245–51. [PubMed: 8835866]

7. Leuschner F, Nahrendorf M. Molecular imaging of coronary atherosclerosis and myocardial infarction: considerations for the bench and perspectives for the clinic. Circ Res. 2011; 108:593–606. [PubMed: 21372291]

8. Sanz J, Fayad ZA. Imaging of atherosclerotic cardiovascular disease. Nature. 2008; 451:953–57. [PubMed: 18288186]

9. Nahrendorf M, Sosnovik DE, French BA, et al. Multimodality cardiovascular molecular imaging, Part II. Circ Cardiovasc Imaging. 2009; 2:56–70. [PubMed: 19808565]

10. Bandettini WP, Arai AE. Advances in clinical applications of cardiovascular magnetic resonance imaging. Heart. 2008; 94:1485–95. [PubMed: 18208827]

11. Hays AG, Hirsch GA, Kelle S, Gerstenblith G, Weiss RG, Stuber M. Noninvasive visualization of coronary artery endothelial function in healthy subjects and in patients with coronary artery disease. J Am Coll Cardiol. 2010; 56:1657–65. [PubMed: 21050976]

12. Kim HW, Farzaneh-Far A, Kim RJ. Cardiovascular magnetic resonance in patients with myocardial infarction: current and emerging applications. J Am Coll Cardiol. 2009; 55:1–16. [PubMed: 20117357]

13. Rehwald WG, Wagner A, Sievers B, Kim RJ, Judd RM. Cardiovascular MRI: its current and future use in clinical practice. Expert Rev Cardiovasc Ther. 2007; 5:307–21. [PubMed: 17338674]

14. Stuber M, Weiss RG. Coronary magnetic resonance angiography. J Magn Reson Imaging. 2007; 26:219–34. [PubMed: 17610288]

15. Catana C, Procissi D, Wu Y, et al. Simultaneous in vivo positron emission tomography and magnetic resonance imaging. Proc Natl Acad Sci U S A. 2008; 105:3705–10. [PubMed: 18319342]

16. Judenhofer MS, Wehrl HF, Newport DF, et al. Simultaneous PET-MRI: a new approach for functional and morphological imaging. Nat Med. 2008; 14:459–65. [PubMed: 18376410]

17. Buscher K, Judenhofer MS, Kuhlmann MT, et al. Isochronous assessment of cardiac metabolism and function in mice using hybrid PET/MRI. J Nucl Med. 2010; 51:1277–84. [PubMed: 20660390]

18. Panizzi P, Swirski FK, Figueiredo JL, et al. Impaired infarct healing in atherosclerotic mice with Ly-6C(hi) monocytosis. J Am Coll Cardiol. 2010; 55:1629–38. [PubMed: 20378083]

19. Yang Z, Berr SS, Gilson WD, Toufektsian MC, French BA. Simultaneous evaluation of infarct size and cardiac function in intact mice by contrast-enhanced cardiac magnetic resonance imaging reveals contractile dysfunction in noninfarcted regions early after myocardial infarction. Circulation. 2004; 109:1161–67. [PubMed: 14967719]

20. Nahrendorf M, Sosnovik D, Chen JW, et al. Activatable magnetic resonance imaging agent reports myeloperoxidase activity in healing infarcts and noninvasively detects the antiinflammatory effects of atorvastatin on ischemia-reperfusion injury. Circulation. 2008; 117:1153–60. [PubMed: 18268141]

21. Kessler ML, Pitluck S, Petti P, Castro JR. Integration of multimodality imaging data for radiotherapy treatment planning. Int J Radiat Oncol Biol Phys. 1991; 21:1653–67. [PubMed: 1938575]

22. Nahrendorf M, Keliher E, Marinelli B, et al. Hybrid PET-optical imaging using targeted probes. Proc Natl Acad Sci U S A. 2010; 107:7910–15. [PubMed: 20385821]

23. Rogers IS, Nasir K, Figueroa AL, et al. Feasibility of FDG imaging of the coronary arteries: comparison between acute coronary syndrome and stable angina. JACC Cardiovasc Imaging. 2010; 3:388–97. [PubMed: 20394901]

24. Nahrendorf M, Swirski FK, Aikawa E, et al. The healing myocardium sequentially mobilizes two monocyte subsets with divergent and complementary functions. J Exp Med. 2007; 204:3037–47. [PubMed: 18025128]

25. Luster AD, Alon R, von Andrian UH. Immune cell migration in inflammation: present and future therapeutic targets. Nat Immunol. 2005; 6:1182–90. [PubMed: 16369557]

26. Swirski FK, Nahrendorf M, Etzrodt M, et al. Identification of splenic reservoir monocytes and their deployment to inflammatory sites. Science. 2009; 325:612–16. [PubMed: 19644120]

27. Leuschner F, Panizzi P, Chico-Calero I, et al. Angiotensin-converting enzyme inhibition prevents the release of monocytes from their splenic reservoir in mice with myocardial infarction. Circ Res. 2010; 107:1364–73. [PubMed: 20930148]

28. Maekawa Y, Anzai T, Yoshikawa T, et al. Prognostic significance of peripheral monocytosis after reperfused acute myocardial infarction:a possible role for left ventricular remodeling. J Am Coll Cardiol. 2002; 39:241–46. [PubMed: 11788214]

29. Mariani M, Fetiveau R, Rossetti E, et al. Significance of total and differential leucocyte count in patients with acute myocardial infarction treated with primary coronary angioplasty. Eur Heart J. 2006; 27:2511–15. [PubMed: 16923741]

30. Tsujioka H, Imanishi T, Ikejima H, et al. Impact of heterogeneity of human peripheral blood monocyte subsets on myocardial salvage in patients with primary acute myocardial infarction. J Am Coll Cardiol. 2009; 54:130–38. [PubMed: 19573729]

31. Wykrzykowska J, Lehman S, Williams G, et al. Imaging of inflamed and vulnerable plaque in coronary arteries with 18F-FDG PET/CT in patients with suppression of myocardial uptake using a low-carbohydrate, high-fat preparation. J Nucl Med. 2009; 50:563–68. [PubMed: 19289431]

32. Peterson LR, Gropler RJ. Radionuclide imaging of myocardial metabolism. Circ Cardiovasc Imaging. 2010; 3:211–22. [PubMed: 20233863]

33. Nahrendorf M, Keliher E, Marinelli B, et al. Detection of Macrophages in Aortic Aneurysms by Nanoparticle Positron Emission Tomography-Computed Tomography. Arterioscler Thromb Vasc Biol. 2011

34. Nahrendorf M, Zhang H, Hembrador S, et al. Nanoparticle PET-CT imaging of macrophages in inflammatory atherosclerosis. Circulation. 2008; 117:379–87. [PubMed: 18158358]
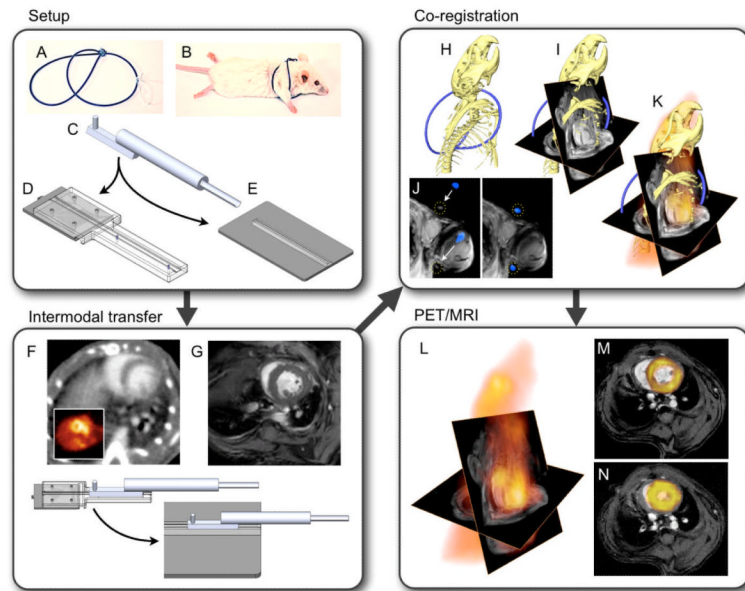
Figure 1. Experimental set up
(A,B) Fiducial vest. (C) Multimodality imaging bed connects to gurneys on PET/CT (D) and MRI (E) to allow for a no-touch transfer of the mouse between modalities (F,G), ensuring that no major position changes hamper data fusion. (H) Three-dimensional CT data show the skeleton and a part of the fiducial marker in blue. (I) CT and MRI matrices are matched, and the angles used during cardiac MRI acquisition are applied. Then, fiducials visible on CT and MRI are aligned (J). (K) Three-dimensional data from PET/CT/MRI. (L) CT information is phased out to yield PET/MRI. (M,N) Double angulated diastolic and systolic PET/MRI short axis views.
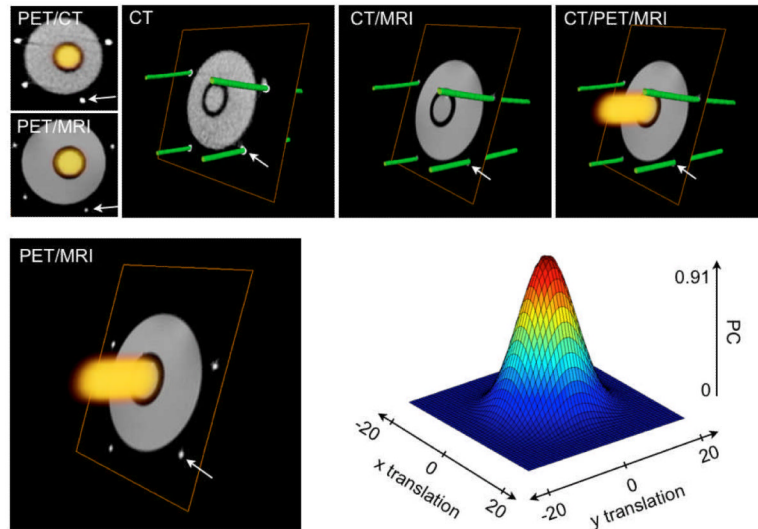
Figure 2. Colocalization
A three-modality phantom was used to assess the developed work flow. Fiducials line the exterior of the phantom, which is composed of two concentric chambers. The outer chamber contains water only, and the inside contains ^{18}F. The mesh diagram displays the correlation of PET and MR signal after fusion. The data sets correlate with a Pearson Correlation Coefficient (PC) of 0.91±0.02. When PET and MRI are translated along the y or x axis, the correlation drops rapidly. Arrows point at fiducial markers.
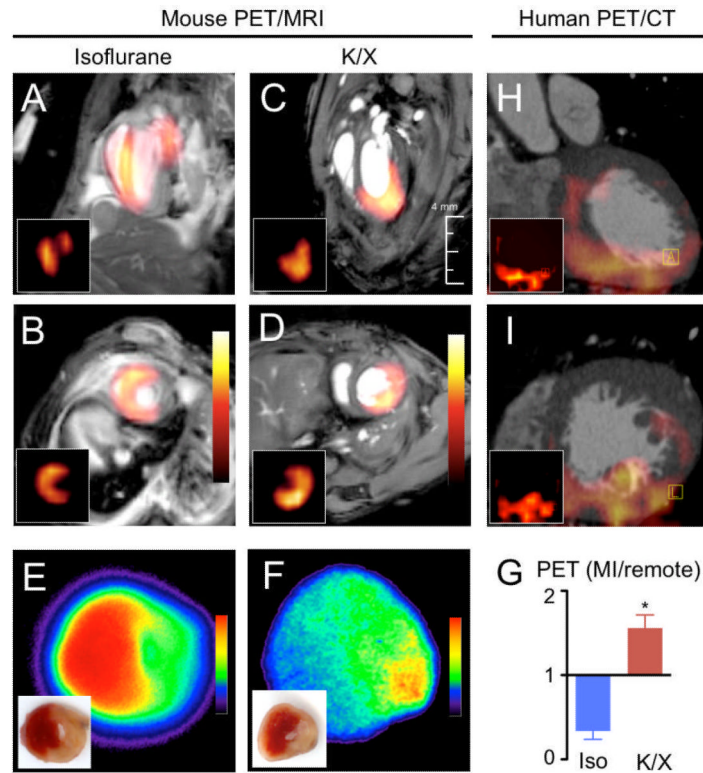
Figure 3. ^{18}FDG PET/GdDTPA MRI

(A-D) ^{18}FDG PET/MRI short and long axis views acquired in mice on day 5 after MI using different anesthesia (K/X: Ketamine/Xylazine). Insets show PET signal. MRI used delayed enhancement cine gradient echo. (E,F) Autoradiography of short axis rings in mice with isoflurane (E) versus K/X (F). Insets depict the infarct as unstained pale tissue on TTC. (G) Infarct to remote myocardium SUV ratio in ^{18}FDG scans with respective anesthesia. Mean ± SEM. *P<0.01. (H,I) ^{18}FDG PET/CT in a patient 5 days after right coronary artery occlusion shows increased PET signal in the injured inferior LV wall.
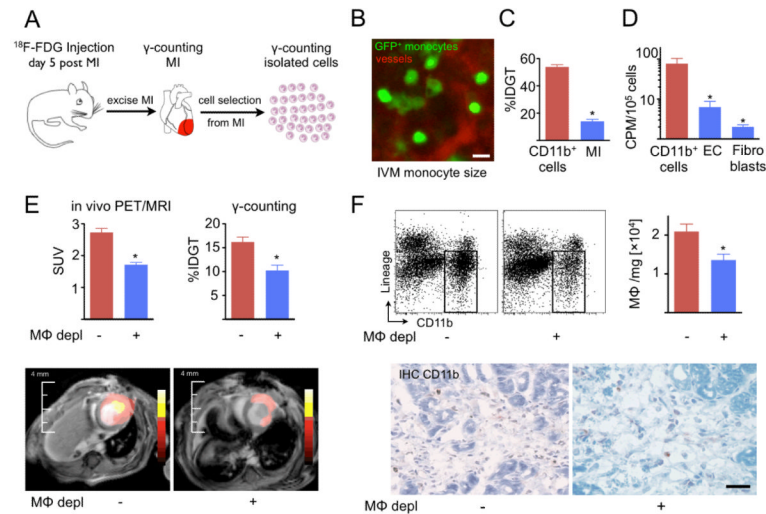
Figure 4. ^{18}FDG uptake is linked to presence of CD11b$^+$ monocytes/macrophages (Mφ)
(A) Experimental set up. Mice were injected, and activity in infarct was assessed by scintillation counting. Thereafter, CD11b$^+$ monocytes/macrophages were isolated from the same infarct tissue by positive selection with antibodies coupled to magnetic beads. (B) To express gamma counts normalized to cellular weight, mean cell diameter was measured by intravital microscopy (IVM). The mean monocytic diameter was then used to calculate cell volume and weight. Scale bar indicates 15μm. (C) Activity of monocytes/macrophages and the tissue from which they were isolated. (D) Counts per minute (CPM) for cell types isolated from infarct tissue (EC: endothelial cells). (E) PET/MRI on day 5 after MI, followed by ex vivo counting. Mφ depl: monocyte/macrophage depletion with clodronate liposomes. (F) FACS enumeration (upper panels) and immunohistochemical staining (lower panels) of monocytes/macrophages in infarcts. Mean±SEM. *P<0.05. Scale bar indicates 30μm.
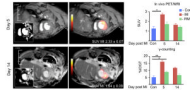
Figure 5. [18]FDG PET/MRI at different time points after MI
Arrows in insets point at infarct in delayed enhancement MRI. Numbers in PET/MR images show the standardized uptake value (SUV) of presented cases. Con: non-infarcted control group. Mean±SEM. *P<0.01.
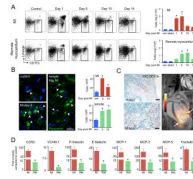
Figure 6. Monocyte/macrophage accumulation in infarct and remote myocardium
(A) FACS analysis of CD11b^{+} cells (gate in dot plots) at different time points in the infarct and remote myocardium. (B) Immunofluorescence microscopy of GFP^{+} monocytes. Scale bar indicates 25μm. Bar graphs show GFP^{+} cells counted per high power field (HPF) at 200x magnification. (C) CD11b^{+} cells are accentuated in the border zone, where we frequently observed high PET signal. Scale bar indicates 0.1mm in upper panel and 30μm in lower panel. On the right, delayed enhancement MRI (inset) and PET/MRI long axis view on day 5 with typical border zone (arrows) configuration of signal. (D) qRT-PCR analysis in infarct (MI) and non-ischemic remote myocardium (RM) on day 5 after MI. Mean±SEM. *P<0.05.
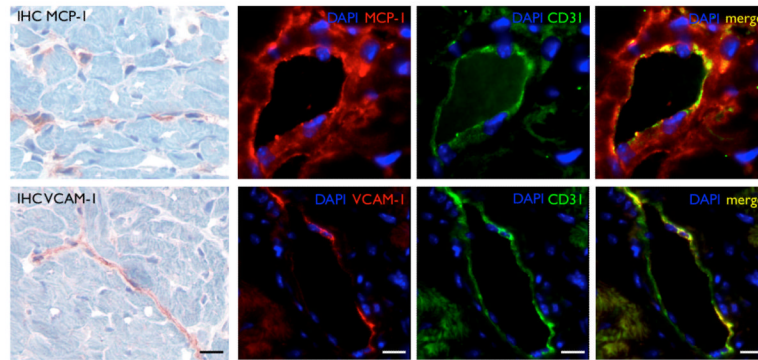
Figure 7. MCP-1 and VCAM-1 expression in remote myocardium
On day 5 after MI, immunohistochemical and immunofluorescence staining show expression of the chemokine and the adhesion molecule, which colocalize with endothelial cells. Scale bar indicates 20μm on immunohistochemical and 10μm on immunofluorescence images.
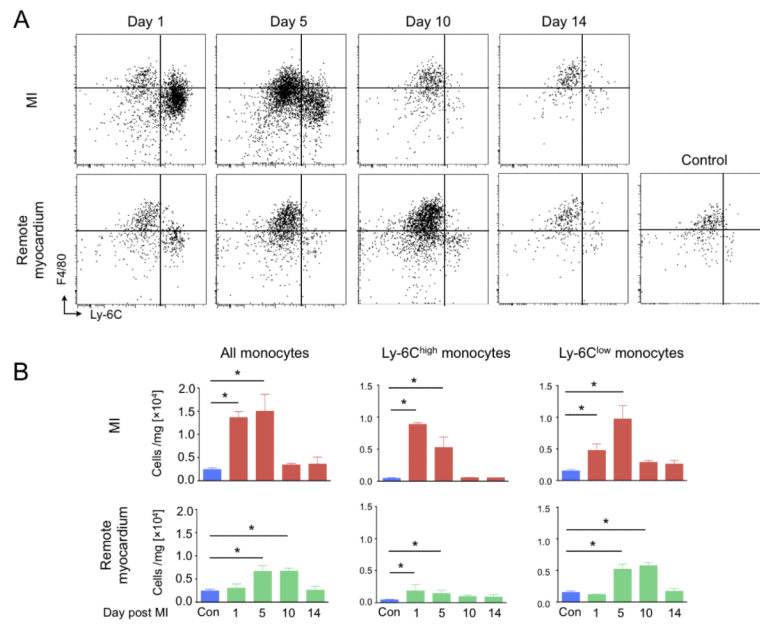
Figure 8. Monocyte subsets in remote myocardium
(A) FACS dot plots gated on CD11b^{+} lineage^{−} cells show serial change of Mφ in MI and remote myocardium. Control: non-infarcted mouse. (B) Bar graphs of absolute number of monocyte subsets in MI and remote myocardium. Mean±SEM. *P<0.05.
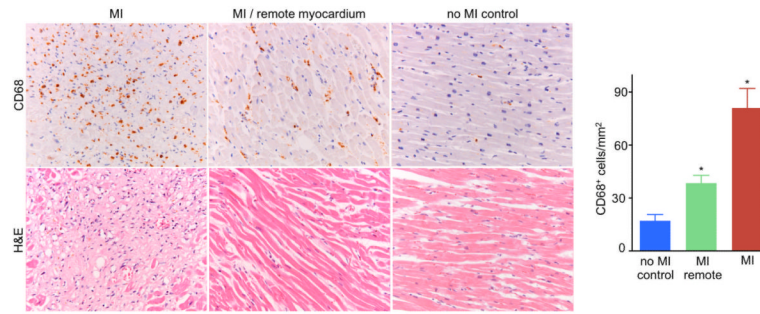
Figure 9. CD68⁺ cells in heart tissue of human patients

Histology images of immunoreactive CD68 staining (top row) and H&E (bottom) at 200X magnification. Mean±SEM. *P<0.05.
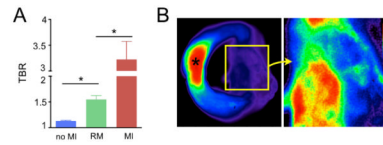
Figure 10. Matrix metalloproteinase activity in remote myocardium
(A) Target to background ratio after injection of protease sensor. Mean±SEM. *P*<0.05. (B)
Fluorescence reflectance image of short axis ring 6 days after MI shows protease sensor
activation in the remote myocardium (inset/right panel). Mean±SEM. *P*<0.05.